Evolution in H 2 O contents during deformation of polycrystalline quartz: An experimental study

Giulia Palazzin, Hugues Raimbourg, Holger Stünitz, Renée Heilbronner, Kai Neufeld, Jacques Précigout

Accepted Manuscript

Evolution in H_2O contents during deformation of polycrystalline quartz: An experimental study

Giulia Palazzin, Hugues Raimbourg, Holger Stünitz, Renée Heilbronner, Kai Neufeld, Jacques Precigout

1   EVOLUTION IN H_2O CONTENTS DURING DEFORMATION OF POLYCRYSTALLINE

2   QUARTZ: AN EXPERIMENTAL STUDY

3   **ABSTRACT**

4   Shear experiments were performed in a Griggs-type apparatus at 800°C and 1.5GPa, at a

5   strain rate of 2.1 x $10^{-5}s^{-1}$ using different starting materials: (i) Powder (grain size 6-10µm) of

6   dry Brazil quartz with 0.15wt% added H_2O, (ii) "dry" Brazil quartz porphyroclasts (grain size

7   ~100-200µm), devoid of fluid inclusions embedded in the same fine grained powder, and (iii)

8   "wet" porphyroclasts (grain size ~100-200µm), containing initially a high density of µm-scale

9   fluid inclusions embedded in the same powder. After hot pressing, samples were deformed to

10   large shear strains (γ~3 to 4.5), in order for the microstructures and H_2O distribution to

11   approach some state of "equilibrium". The H_2O content and speciation in quartz were

12   analyzed by Fourier Transform Infra-Red (FTIR) spectroscopy before and after the

13   experiments. Mechanical peak strength is generally lower in experiments with 100% hydrated

14   matrix, intermediate in experiments incorporating wet porphyroclasts (with a proportion of 30

15   or 70%) and highest in those with dry porphyroclasts. All experiments with porphyroclasts

16   show pronounced strain weakening, and the strengths of most samples converge to similar

17   values at large strain. Wet porphyroclasts are pervasively recrystallized during deformation,

18   while dry porphyroclasts recrystallize only at their rims and remain weakly deformed.

19   Recrystallization of the initially fluid-inclusion-rich porphyroclasts results in a decrease in

20   inclusion abundance and total H_2O content, while H_2O content of initially dry clasts increases

21   during deformation. H_2O contents of all high strain samples converge to similar values for

22   matrix and recrystallized grains. In samples with wet porphyroclasts, shear bands with high

23   porosity and fluid contents develop and they host the precipitation of euhedral quartz crystals

24   surrounded by a free-fluid phase. These high porosity sites are sinks for collecting H_2O in

25   excess of the storage capacity of the grain boundary network of the recrystallized aggregate.

26   The H_2O storage capacity of the grain boundary network is determined as a H_2O-boundary-

27   film of ~0.7 nm thickness.

28   **1. INTRODUCTION**

29   Quartz weakening by H_2O is well known since the seminal papers by Griggs and Blacic

30   (1965) and Griggs (1967). In natural rocks, it is tacitly assumed that quartz is sufficiently

31   "wet", because quartz usually is one of the weakest components in plastically deformed rocks.

32   However, some recent observations have described potentially drier natural rocks, which are

33   deformed (Fitzgerald et al., 2006, Menegon et al., 2011, Kilian et al., 2016). On the other

34   hand, there is clear evidence for shear zones involving material initially rich in H_2O

35   (principally in the form of fluid inclusions), such as metasediments along the subduction plate

36   interface (Palazzin et al., 2016; Raimbourg et al., 2018; Raimbourg et al., 2015, Saffer and

37   Tobin, 2011), and the final deformed rocks do not necessarily indicate high H_2O contents.

38   Thus, the introduction or reduction of H_2O in quartz in natural rock deformation remains one

39   of the great unknown parameters.

40   As pointed out by Griggs (1967), the H_2O weakening effect in quartz may combine different

41   elementary processes, which all contribute to enhance plastic deformation. One process is

42   related to the enhanced intra-crystalline plasticity of quartz. It has been extensively studied in

43   single crystals, most of them synthetic (Griggs, 1967, 1974; Griggs and Blacic, 1965;

44   Kekulawala et al., 1978, 1981; McLaren et al., 1983; McLaren et al., 1989). The microscopic

45   weakening phenomenon may eventually depend on the hydrolysis of Si-O bonds in the cores

46   of dislocations (Griggs, 1974), on enhanced climb of dislocations (Cordier and Doukhan,

47   1989; Mainprice and Jaoul, 2009; Tullis and Yund, 1989), or involve the increased dislocation

48   nucleation at nano-scale H_2O clusters acting as dislocation sources (Fitz Gerald et al., 1991;

49   McLaren et al., 1989). H_2O, in the form of molecular H_2O is most efficient to weaken quartz

50   single crystals (e.g., Paterson, 1989, Kekulawala et al., 1978, 1981). However, the growth of

51   nano-scale clusters of H_2O to form larger fluid inclusions, resulting from heat treatment,

52   increases quartz strength (Kekulawala et al., 1978): milky quartz containing a large

53   concentration of H_2O confined in µm-scale fluid inclusions is stronger than synthetic crystal

54   with a much lower H_2O concentration. The effect of OH structural defects on deformation is

55   unclear but appears limited (Doukhan and Trépied, 1985; Paterson, 1989; Kronenberg, 1994;

56   Cordier et al., 1994). However, in a given quartz material, the weakening effect increases with

57   the H_2O content (Griggs, 1967, Blacic and Christie, 1984, Kronenberg and Tullis, 1984,

58   Cordier and Doukhan 1989, Hirth and Tullis 1992, Den Brok et al.,1994, Stunitz et al., 2017).

59   Another elementary process, proposed by Griggs (1967) as a cause of quartz hydrolytic

60   weakening, is recrystallization, which operates in polycrystals (Jaoul et al., 1984; Tullis and

61   Yund, 1989; Hirth and Tullis, 1992). Similar to single crystals, in quartz aggregates, there is

62   an inverse correlation between the amount of added H_2O and the assemblage strength (Jaoul

63   et al., 1984; Kronenberg and Tullis, 1984). In particular, in H_2O-rich experiments, the small

64   grain sizes decrease strength, suggesting some contribution of grain-boundary mediated

65   process to weakening (Kronenberg and Tullis, 1984).

66 The case of deformation of polycrystalline material is of prime interest to nature, as it directly

67 applies to the strength of mylonites and ultramylonites. It involves the combination of

68 intracrystalline and grain boundary processes, so that identifying the H_2O-weakening effect is

69 difficult. In addition, natural material may contain H_2O concentrations varying over several

70 orders of magnitude (Ito and Nakashima, 2002): microcrystalline cherts, non-metamorphic or

71 of diagenetic grade, contain up to ~40,000 $H/10^6Si$. In contrast, the threshold for the onset of

72 weakening, in other words the boundary between wet and dry quartz in experiments on

73 synthetic quartz, is ~100 $H/10^6$ Si (Griggs and Blacic, 1965; Cordier and Doukhan, 1991, Den

74 Brock, 1994; Christie et al., 1964, Kilian et al., 2016). Not all of the H_2O content of natural

75 quartz (primarily in µm-scale fluid inclusions) has a weakening effect (Kekulawala et al.,

76 1978), but the mechanical role of large H_2O concentrations is still to be determined.

77 In particular, considering natural quartz as a two-phase-system of crystal and fluid inclusions,

78 the transfer of H_2O from the inclusions into the crystal (and the associated weakening) is

79 difficult because of the very low solubility and diffusive flux of H_2O in quartz (Kronenberg et

80 al., 1986, Paterson 1986, Gerretsen et al., 1989). As a consequence, micro-fracturing

81 (Kronenberg et al., 1986, 1990, Gerretsen et al., 1989, FitzGerald et al., 1991, Stunitz et al.,

82 2017) and diffusion (along subgrain boundaries or dislocation cores; Post and Tullis, 1998)),

83 as well as grain boundary migration (Gleason and DeSisto, 2008), have been proposed as

84 mechanisms responsible for H_2O uptake, because oxygen diffusion may be increased along

85 dislocations or grain boundaries.

86 Finally, H_2O concentration is not a fixed quantity and depends itself on deformation, as

87 recrystallization redistributes H_2O within the material. For example, in rock of low

88 metamorphic grade from Japanese accretionary complexes, the H_2O concentration decreases

89 with increasing grade, reflecting the progress of recrystallization (Ito and Nakashima, 2002).

90 In grains with a large initial H_2O content stored in fluid inclusions, the migration of grain

91 boundaries that accompanies recrystallization leads to the loss of most fluid inclusions and the

92 decrease H_2O concentration (Bakker and Jansen, 1994; Kilian et al., 2016; Palazzin et al.,

93 2016). Therefore, the "steady-state" H_2O concentration (and the associated strength) in a

94 deforming and recrystallizing aggregate is poorly known. FTIR measurements in natural

95 mylonites formed at mid-greenschist and amphibolite facies conditions show low H_2O

96 contents, <100 to ~320 $H/10^6$ Si at grain boundary regions (Gleason and DeSisto, 2008) and

97 in individual single grains (Kilian et al., 2016).

98 Given the wealth of existing experimental and natural studies on H_2O weakening of quartz,

99 this study specifically focuses on the strength of quartz as a function of H_2O-content. Another

100 aspect of this study is the evolution of H_2O-content (i.e. increasing and decreasing H_2O

101 contents in deforming polycrystals). "Wet" initial conditions (e.g., applicable to examples to

102 sediments in subduction settings) and dry initial crystals are compared and their H_2O-

103 evolution studied. We have carried out high strain experiments in order to simulate natural

104 shear zones but also to be as close as possible to steady-state conditions, both in terms of

105 microstructures and H_2O distribution. We focused on the role of H_2O on recrystallization and

106 the effect of H_2O content and speciation.

107 **2. METHODS**

108 **2.1 Experimental procedure**

109 All experiments were performed in a Griggs-apparatus at 800°C, ~1500 MPa and a constant

110 strain rate of ~2 $x10^{-5}$ s^{-1}. These conditions were chosen in order to activate dislocation creep

111 in the samples (cf. Hirth and Tullis, 1992). Pre-cut (at 45°) Al_2O_3 pistons were inserted into a

112 pre-annealed platinum jacket. A ~1mm thick layer of fine quartz matrix powder was placed

113 between pistons, which contained a fixed proportion of larger grains ("porphyroclasts"). The

114 matrix material (Brazil quartz) was the same in all experiments while two distinct types of

115 porphyroclasts were used.

116 The quartz matrix comes from a dry Brazil single-crystal crushed in a stainless steel mortar.

117 After crushing, we applied repeated cycles of sedimentation in a H_2O column to sort grains

118 of a specific size. The powder we obtained consisted of grains with a diameter in the range of

119 ~6-20µm, although a small fraction of the grains (~15% in volume), had larger, up to 110µm,

120 diameter.

121 The first material chosen for the porphyroclast was dry Brazil quartz. A single euhedral

122 crystal of ~4 cm long was cut, trying to avoid optically visible secondary fluid inclusions

123 planes. Porphyroclasts were obtained by crushing the selected part of the crystal in a stainless

124 steel mortar and separating a size in the range of 200-250 µm by sieving.

125 The second porphyroclast material was milky vein quartz from the Hyuga mélange, a low-

126 grade metamorphic unit from the Shimanto Belt in Japan (Raimbourg et al., 2014; Palazzin et

127 al., 2016 for detailed description). Fragments from mm-wide veins were crushed in an agate

128 mortar and quartz was separated from the remaining matrix by a Frantz magnetic separator

129 and density (Sodium Polytungstate) techniques. The material was sieved to separate the 200-

130 250 µm size fraction. A final hand-picking was carried out to avoid possible clay mineral

131 contamination.

132 The matrix and porphyroclasts were dried at 110°C for 48 hours before preparing the mixture.

133 Four experimental samples were prepared by mixing 30% and 70% porphyroclasts of either

134 Hyuga or Brazil quartz with the pure Brazil quartz matrix. In addition, one sample with 100%

135 pure Brazil matrix was deformed.

136 To ensure an homogenous distribution of clasts in the matrix, we added acetone to the

137 clasts+matrix mixture in a glass beaker and stirred the slurry obtained in an ultrasonic bath,

138 until complete acetone evaporation (cf. de Ronde et al. (2005). The porphyroclasts and matrix

139 quartz mixtures were dried at 110°C and then placed on the lower Al_2O_3-piston surface after

140 adding distilled water with a micropipette. The material was wrapped in Ni-foil inside the Pt-

141 jacket. The amount of water was adjusted to the proportion of the matrix (100, 70 or 30%),

142 corresponding to an H_2O-content of 0.15 wt.% for matrix (**Table 1**). The second pre-cut

143 piston was placed on top of the sample, and the Pt jacket was welded with a Lambert

144 precision point welder. The sample was then placed in the center of a graphite furnace inside

145 the solid confining medium (NaCl). The sample-piston assembly is illustrated in **Figure 1a**.

146 Pumping and heating were performed slowly to reach the desired temperature and pressure

147 conditions (normally over ~9 hours). Confining pressure was initially increased to 150 MPa

148 before heating. Temperature was increased in steps of 100°C at a rate of 25°C per minute at

149 pressure intervals of several hundreds of MPa. When pressure and temperature were at 1.5

150 GPa and 800°C, axial piston movement was started at a constant displacement rate. The

151 typical time to reach the hit point was ~20 to 24 hrs. During this stage, the sample was

152 effectively subjected to hot isostatic pressing, leading to a denser aggregate.

153 The hit point, marked by a sharp increase in axial force, corresponds to the onset of sample

154 loading and deformation. Axial force then rises rapidly to a maximum value ("peak stress").

155 The subsequent deformation of the sample, up to γ ~4-6, is achieved for near constant, or

156 slowly decreasing axial force.

157 At the end of each experiment, the sample was quenched to a temperature of 200°C within 3

158 minutes. Subsequently, the confining pressure was lowered to room pressure over a period of

159 several hours, keeping a differential stress of (initially) 100-200 MPa on the sample in order

160 to minimize unloading cracks.

161 Some samples were kept under hydrostatic conditions without deformation to obtain

162 information of the microstructures during the initial steps of the experiments. All samples

163 were cut along their long axis normal to the shear zone in order to provide thin and thick

164 sections for microscopy and FTIR analysis, respectively.

2.2 FTIR measurements

166 To enable analysis of the H_2O-content, slices of the single Brazil quartz crystal (cut in the

167 direction normal to the [c]-axis) and isolated porphyroclasts of Hyuga quartz (both

168 corresponding to the starting material) were firstly embedded in orthodontic acrylic resin

169 (Vertex Orthoplast) and then manually doubly polished (thickness 120-140 µm). Deformed

170 samples were cutted and directly polished to 120-140 µm thick sections. All samples were

171 then accurately cleaned in ultrasonic bath with acetone to remove remaining resin. The H_2O-

172 content was determined by Fourier Transform Infrared (FTIR) spectroscopy with a

173 microscopic FTIR continuum spectrometer (Nicolet-6700, Thermo Scientific) at the Institut

174 des Sciences de la Terre d'Orléans (France). All the measurements were carried out at

175 atmospheric temperature, after purging the optical path of the IR beam with dry air in order to

176 avoid measurement of atmospheric water. A sodium chloride window was used to collect and

177 subtract the background for each measurement. A 50×50 µm aperture window was used for

178 all the analyses. 256 scans per spectrum were collected with 4 cm^{-1} resolution. We estimated

179 the concentration of "molecular" H_2O, using the Paterson (1982) calibration of the integral

180 absorption band between ~2800 and 3780 cm^{-1} using the Beer-Lambert law,

181 $A = C * t * e$

182 where C is the concentration, t the thickness, and e the integrated molar absorption coefficient

183 $(0,8120 \ L \ cm^{-2} \ mol^{-1})$. Sample thicknesses t was obtained from the height of the peak at 1790

184 cm^{-1} corresponding to the Si–O band, again making use of the Beer-Lambert law (e.g., Ito and

185 Nakashima, 2002). H_2O concentration (wt. ppm H_2O/SiO_2) was obtained (**Table 1**) by

186 dividing the $H/10^6Si$-value of the Paterson (1982) calibration by a factor 6.67 given in Kilian

187 et al. (2016).

2.3 EBSD - CIP - Grain Size determinations

189 Crystallographic preferred orientation (CPO) of quartz was measured by electron backscatter

190 diffraction (EBSD) (Lloyd and Freeman, 1994; Prior et al., 1999) and by computer integrated

191 polarized (CIP) microscopy (Heilbronner and Barrett, 2014). EBSD patterns were acquired

192 with an Oxford AZTEC system and a Nordlys detector on a FE- Zeiss Merlin compact SEM

193 at the University of Tromsø. We used thin sections with a thin carbon coat at 70° tilt angle, 20

6

194   kV acceleration voltage, □10 nA beam current, and 11 to 14 mm working distances at a step

195   size of 0.1 µm. Initial noise reduction was performed with CHANNEL 5 software by

196   removing isolated points and replacing non-indexed points with the orientation of their

197   neighbors (interactively filled starting with eight similar neighbors down to six or five similar

198   neighbors). Thin sections were rotated 45° counterclockwise in order to align shear zone

199   boundaries (forcing block interface) to reference frame direction. Data were analyzed with

200   MTEX toolbox (Hielscher and Schaeben, 2008). Analysis of the grain boundary fraction was

201   carried out using EBSD maps. Grains were segmented based on c-axis misorientation after

202   converting EBSD images to CIP images using a procedure described in Heilbronner and

203   Kilian (2017).

204   **3. RESULTS**

205   **3.1 Characterization of the starting material**

206   Hyuga quartz has a milky appearance due to the great abundance of many tiny fluid

207   inclusions (Palazzin et al., 2016). These inclusions range from a few to 10µm in diameter

208   (Raimbourg et al., 2015) and are heterogeneously distributed in the porphyroclasts which look

209   dark in thin section and grain mounts (**Figure 1b-1**). As shown by FTIR spectra**,** OH content

210   is variable as a consequence of the distribution of fluid inclusions (**Figure 1b-1**). Mean

211   measured values (listed in **Table 1**) are of the order of ~23,000 $H/10^6Si$, or ~0.34wt% H_2O,

212   which is about twice the amount of H_2O added to the sample matrix. After the rise in T and P

213   up to 800°C

214   and 1.5GPa, Hyuga porphyroclasts show a lower abundance of fluid inclusions than the

215   starting material, so that they appear clearer (**Figure 1b-2**). The measured amount of OH is

216   lowered to about half of the initial quantity (~12,000 $H/10^6Si$), corresponding to ~0.18wt%,

217   similar to the added H_2O content of 0.15wt% (**Table 1**, **Figure 1b-2**).

218   Porphyroclasts of dry Brazil quartz are optically strain free and contain no fluid inclusions

219   (**Figure 1b-3**). The mean measured H content in Brazil quartz is about 260 $H/10^6Si$ and

220   confirms that this material can be considered as "dry" quartz for deformation (**Table 1**; Post

221   and Tullis, 1998; Paterson, 1989)**.**

222   **3.2 Mechanical data**

223   Moderate peak shear stress and lower flow strength values (**Figure 2, Table 2**) indicate

224   dominant plastic deformation in most samples at the applied strain rate of ~2.1 x 10^{-5} s^{-1}. Only

225   the 70% Brazil clasts sample reaches peak stress above the Goetze criterion ($\Delta\sigma$ = 1600 MPa

7

226 at gamma ~2; **Figure 2**) for plastic deformation ($\Delta\sigma \approx P_{conf}$; Kohlstedt et al., 1995), all other

227 samples are in the fully plastic regime. All curves are characterized by a first stage of a rapid

228 increase in stress up to peak values ($\gamma = 0$ to ~0.5/1.5), followed by a weakening stage that

229 may or may not reach steady state stress values.

230 Two samples with 100% matrix show a ~50% difference in peak stress (at γ ~0.8) and a

231 smaller difference at γ ~3.5 (**Figure 2**). The sample with 30% Hyuga porphyroclasts shows a

232 peak shear stress between that of the two matrix samples (**Figure 2**) and a final stress value

233 that is almost identical to that of the matrix sample (~260 MPa) at γ ~3.2. The sample with

234 70% Hyuga porphyroclasts shows a considerably higher peak stress but weakens to a similar

235 finite strength as the 30% Hyuga and matrix samples.

236 Samples with Brazil porphyroclasts reach higher peak shear stresses than their Hyuga

237 porphyroclasts counterparts: up to ~650 MPa for 70% clasts and ~420 MPa for 30% Brazil

238 clasts. After the peak stress, all matrix + clasts assemblages display significant weakening

239 with a similar slope, irrespective of the nature of the clasts. It is remarkable that the flow

240 stresses of three assemblages, containing 70% and 30% of Hyuga porphyroclasts and 30% of

241 Brazil porphyroclasts, converge towards a common flow stress of ~250-280 MPa at γ ~3.3

242 (**Figure 2**), similar to the 100% matrix, regardless of their peak stress values.

243 **3.3 Microstructural observations**

244 **3.3.1 Hot pressed material**

245 After hot-pressing, only little porosity is observed, typically at triple junctions of grains

246 (**Figure 3**). Pores rarely exceed 1μ diameter, and total porosity is estimated to be ~ 2 to 4 %

247 of the sample volume. Very few open grain boundaries are present, but these are

248 approximately normal to the piston axis, so that they probably result from quenching and

249 unloading (**Figure 3**).

250 **3.3.2 Pure matrix deformation**

251 The deformed samples with pure 100% matrix are characterized by pervasive recrystallization

252 of the deformed parts of the samples. Strain is partitioned into narrow regions at the piston

253 ends, extending into a broader region, which occupies almost the full width of the shear zone

254 in the center (**Figure 1a**). The quartz grains in the regions of strain localization show a strong

255 shape fabric, and individual grain boundaries are difficult to detect in the high strain regions

256 in the light microscope because of their strong CPO (see paragraph 3.5.1).

257

3.3.3 Matrix + Brazil porphyroclasts

In these samples, a foliation results from the elongation of matrix domains and recrystallized regions extending from porphyroclasts at an angle of about 18° to the shear zone boundaries (piston interfaces; **Figure 4a,b**). In the sample with 70% clasts, tails of recrystallized quartz (**Figure 4b,d**) extending from porphyroclasts define σ-type clasts (Hanmer, 1984b; Passchier and Simpson, 1986). Porphyroclasts in the assembly with 30% clasts show a variable shape: some are elongated, while others have an equant shape, both of which are mainly inherited from their pre-deformation state (**Figure 4a,c**). Porphyroclasts contain few or no subgrains. Their rims are commonly sutured and their cores are surrounded by small recrystallized grains (**Figure 4c,d**). Some undulatory extinction and deformation lamellae are common (**Figure 5a,b).** These microstructures are characteristic of dislocation creep regime 1 described by Hirth and Tullis (1992). In both Brazil clast samples the extent of recrystallization of porphyroclasts is limited, and relict clasts and recrystallized rims are easy to distinguish (**Figure 4-5a,b**).

3.3.4 Matrix + Hyuga porphyroclasts

Hyuga porphyroclasts (6**a,b**) invariably are strongly elongated, up to an aspect ratio of ~10. Their shape fabric defines a foliation at about 10° to the shear zone boundaries. They are extensively recrystallized into elongated grain aggregates, with serrated boundaries, and subgrains, forming a microstructure of dislocation creep regime 2 of Hirth and Tullis (1992). Because of the penetrative recrystallization, former porphyroclasts are difficult to distinguish from the surrounding matrix (**Figs 5c,d and 6c**), except for the fact that porphyroclasts recrystallized and grown into larger grains and subgrains than the matrix (**Figs 5c,d and 6c,d**). The clasts in the 70% Hyuga porphyroclasts sample are more pervasively recrystallized than in the 30% clasts sample, possibly due to higher strain.

3.3.5 Shear Bands

In both samples containing Hyuga porphyroclasts, shear bands develop oblique to the shear zone boundaries in a synthetic orientation (c´-orientation) with the imposed shear sense (**Figs 6c,d and 7**). The angle between these planes and the shear zone boundary varies between ~25 and ~35°. The stretched porphyroclasts define the S-planes of a SC' fabric (C-planes are absent). Plane polarized light images show the shear bands as trails of small fluid inclusions (**Figure 7a**). The shear bands are most ubiquitous in the sample containing 70% of Hyuga porphyroclasts, where the bands cut across the matrix and the stretched porphyroclasts, making an average angle of 27 degrees with porphyroclast long axes. SEM images (**Figure

9

291   **7c**) show that the C' bands are zones of high porosity, composed of cube-shaped, idiomorphic

292   grains, of size ~2-5 µm, surrounded by voids.

293   **3.4 H$_2$O content/distribution**

294   **3.4.1 Matrix**

295   The original Brazil quartz crystal, from which the matrix was produced, contains a very low

296   proportion of H$_2$O, of the order of ~250 H/10^{6}Si (**Table 1 and Figure 1b-3**). In each

297   experiment, H$_2$O had been initially added to the dry Brazil quartz matrix, with a proportion of

298   0.15wt%, or equivalently 10 000 H/10^{6}Si.

299   After the experiments, the matrix displays a broad absorption band in the region between

300   3000 and 3800 cm^{-1} (**Figure 8a**), representing the molecular H$_2$O in quartz and in the grain

301   boundaries. From this broad absorption band, the H$_2$O content after experiments can be

302   estimated as ~900 to 2900 H/10^{6}Si in deformed samples and ~4200 H/10^{6}Si in an undeformed

303   sample (464GP, **Table 1**). The water initially added has been retained to variable extent in the

304   matrix during the application of pressure and temperature and later deformation.

305   The same initial material (Brazil quartz matrix + 30% Hyuga porphyroclasts) was brought to

306   high P and T in one experiment and then retrieved (464GP). In another experiment it was

307   deformed to high strain (428GP). The Brazil matrix in the deformed sample contains ~1500

308   H/10^{6}Si, i.e. 2 to 3 times less than the corresponding experiment without deformation (~4200

309   H/10^{6}Si; **Table 1**).

310   Comparing the different experimental materials, the H$_2$O content of the matrix is

311   significantly higher for experiments containing initially "wet" Hyuga porphyroclasts (~1500

312   for 30% and ~2900 H/10^{6}Si for 70% porphyroclasts) than in experiments containing initially

313   "dry" Brazil porphyroclasts (~950 and ~1300 H/10^{6}Si for 30% and 70% of porphyroclasts) or

314   experiments with 100% matrix (~800 H/10^{6}Si) (**Figure 8a, Table 1**). Additionally, in

315   experiments containing Hyuga porphyroclasts, the H$_2$O -content of the quartz matrix and that

316   of the recrystallized Hyuga clasts are similar after deformation, considering the large standard

317   deviation: with 30% of clasts, the matrix contains ~1500 H/10^{6}Si and porphyroclasts ~2300

318   H/10^{6}Si, while for 70% clasts, the matrix contains ~2900 H/10^{6}Si and porphyroclasts ~2350

319   H/10^{6}Si (**Table 1**).

320   All spectra show discrete absorption bands at 3363, 3382, and 3595 cm^{-1}, which were not

321   present in the original Brazil quartz spectra (cf. **Figures 1D and 8**). The most prominent

322   discrete absorption band in the deformed matrix measurements is at 3595 cm^{-1}.

3.4.2 Porphyroclasts

Hyuga porphyroclasts display a broad absorption band in the region between 3000 and 3800 cm^{-1} (**Figures 1b,c,d and 10a**), which is related to molecular H_2O contained in the large number of fluid inclusions initially present. During hot pressing the broad band of molecular H_2O shows a general decrease with respect to the as-is material. This reduction in water content is enhanced with deformation, as Hyuga porphyroclasts in deformed samples contain ~1/10 of their initial water content (**Table 1, Figure 9a**).

In addition to this evolution of the H_2O content, the shape of the H_2O spectrum is also modified by the application of P-T conditions and deformation from a broad triangular absorption centered around around 3400cm^{-1} that is charateristic of fluid H_2O to a very broad flat flat shape absorption (**Figure 9a**) that is unlike absorption spectra of liquid H_2O. The position of discrete absorption bands, related to structurally-bound H_2O, are also modified. The initial spectrum displays only a discrete absorption band at 3382 cm^{-1}. Application of P-T condition results in the development of a band at 3585cm^{-1}, while after deformation a discrete band around 3595cm^{-1} appears as well. As a result of this evolution in shape and integrated area, recrystallized Hyuga porphyroclasts and the fine grained matrix converge towards a similar IR spectrum (**Figure 9b**).

Initially, Brazil porphyroclasts contain virtually no H_2O (~250 H/10^{6}Si), resulting in a flat absorption spectrum (**Figure 8b**), where only one secondary absorption band at 3485 cm^{-1} is visible. The application of P-T conditions and deformation (**Figure 10, Table 1**) results first in the increase in H_2O content in the cores of the porphyroclasts (~650 H/10^{6}Si) and in their recrystallized rims (~1500 for 30% and ~900 H/10^{6}Si for 70% of porphyroclasts). The very weakly deformed cores, showing only undulatory extinction, contain a smaller amount of H_2O (**Figure 10b,c,f**) than observed for the recrystallized regions with their grain boundaries (**Figure 10d,e,f**). Furthermore, new discrete absorption bands appear at 3595 cm^{-1} and at 3363 cm^{-1} in the recrystallized region, whereas the core shows a discrete band at 3585 cm^{-1}, which is absent in the recrystallized region (**Figure 10a,f**).

3.4.3 Shear bands

In the experimental sample containing 30% of Hyuga porphyroclasts, the shear bands that cut across porphyroclasts and matrix contain a high H_2O concentration of ~3700 H/10^{6}Si (**Table 1**). This H_2O content is significantly higher than either porphyroclasts (~2300 H/10^{6}Si) or the matrix (~1500 H/10^{6}Si) that hosts these bands. It corresponds to trails of fluid inclusions

355 (optical observations) and the presence of abundant voids (SEM observations) along the shear

356 bands (**Figure 7a,c**).

357 **3.5 Crystallographic fabrics**

358 Grain boundary maps, orientation images and pole figures are derived from EBSD maps and

359 shown for a pure matrix sample and for one sample containing 70% Hyuga and one with 70%

360 Brazil clasts. For easier interpretation, the orientation images are recalculated as c-axis

361 orientation images (see color look-up table on the right of **Figs 11b-12b and 13b**).

362 **3.5.1 100% Matrix**

363 In the 100% matrix experiment, the central region of pervasive recrystallization of the sample

364 shows elongated grains, whose long axes are oriented at ~25 degrees (on average) from the

365 shear plane (**Figure 11a,b**). Their CPO shows a well-defined maximum rotated synthetically

366 with the sense of shear, and all crystallographic axes are concentrated in or near the X-Z plane

367 (**Figure 11c**).

368 **3.5.2 Recrystallized Hyuga porphyroclasts CPO**

369 EBSD map shows that a large proportion of initial Hyuga porphyroclasts, strongly elongated

370 after deformation, consists of recrystallized grains with small grain size (light blue domain,

371 **Figure 12a,b**).

372 The CPO shows a similar asymmetry with respect to the shear plane as the 100% matrix.

373 Parts of the recrystallized regions show many subgrain boundaries in a rather uniform CPO

374 domain (**Figure 12b**).

375

376 **3.5.3 Recrystallized tail of a Brazil porphyroclast**

377 In the experiment with 70% Brazil quartz, the crystallographic fabric of the recrystallized tail

378 is qualitatively similar as that of the 100% matrix, but the grain size distribution is broader

379 (**Figure 13a,b**). The c-axis maxima are slightly weaker (**Figure 13c**). The recrystallized tail

380 appears to have a better developed CPO than the matrix (orange domain, **Figure 13b**).

381 **3.5.3 Shear bands and strain shadows**

382 Shear bands are developed only in Hyuga clast samples. CIP analysis of these samples reveals

383 that shear bands inside larger porphyroclasts have a completely different c-axis orientation

384 from that of the surrounding material, as seen in light microscope images with the

385 compensation plate inserted (**Figure 7b**). Strain shadows around Brazil porphyroclasts

386 constitute other high-porosity domains where small idiomorphic grains are surrounded by

387 voids, and the crystallographic orientation of these small grains, similar to that of shear bands,

388 is very different from surrounding quartz. The strong contrast in orientation between the

389 grains in shear bands and pressure shadows and the surrounding material, the high-porosity,

390 and the grain shapes suggest that these grains formed as a result of precipitation in a fluid

391 filled porosity.

4. DISCUSSION

4.1 Mechanical Data

394 After exhibiting an initial peak stress, all samples deform at flow stresses well below the

395 values of the confining pressure (**Figure 2**; Goetze Criterion: Kohlstedt et al., 1995). The

396 inference of the Goetze Criterion that fractures opening and extension are suppressed when Pc

397 > differential stress is consistent with the fact that none of our samples contained

398 thoroughgoing fractures. The 100% Brazil quartz matrix samples show a higher flow stress

399 than that of wet polycrystalline quartz of Hirth and Tullis (1992) in coaxial experiments at the

400 same temperature and confining pressure. The shear strain rate of our experiments is faster

401 than the coaxial strain rate of Hirth and Tullis (1992), which may explain the differences.

402 From the mechanical data it is clear that the originally dry Brazil quartz matrix material has

403 become fully "wet" during pressurization and heating, as it has been achieved in experiments

404 previously by Post and Tullis (1998) and Rutter and Brodie (2004a).

405 All samples with porphyroclasts show a pronounced peak stress and subsequent weakening

406 behavior, consistent with a higher initial strength of the large porphyroclasts, which

407 subsequently weaken during recrystallization. Even the Hyuga quartz, which contains a lot of

408 H_2O in the form of aqueous fluid inclusions and thus may be expected to be weaker than the

409 pure Brazil quartz matrix, shows this behavior. The mechanical evolution of the sample raises

410 two points: (1) Porphyroclast material shows pronounced strain weakening, probably caused

411 by recrystallization (2) Fine grained quartz material tends to be weaker than that with coarse

412 grained porphyroclasts. The former point has already been addressed by Hirth and Tullis

413 (1992), who have observed strain weakening behavior for dislocation creep regime 1. The

414 weakening is attributed to local grain boundary migration (bulging recrystallization) of more

415 or less undeformed porphyroclasts. In our examples here, dynamic recrystallization takes

416 place by progressive subgrain rotation (see below), so that the recrystallization mechanism

417 does not seem to be the only controlling factor for the weakening.

418 Steady state is reached by the 30% Hyuga material (428GP) after $\gamma \approx 1.5$ (**Figure 2**). The 70%

419 Hyuga sample (456GP) reaches similar stresses as the 30% sample, but at higher gamma

420 values and after higher peak stress. The grain sizes of the 70% Hyuga sample are smaller,

421 even though the finite stress values of the samples are identical. The findings are consistent

422 with the results by Kidder et al. (2016), who find that the recrystallized grain size is

423 dependent on stress history.

424 Samples with dry Brazil porphyroclasts do not reach steady state after $\gamma = 3.5$ or 4 is

425 consistent with Brazil clasts behaving as more rigid particles, and their recrystallization takes

426 more strain than does recrystallization of the Hyuga clasts. The high peak strength of the 70%

427 Brazil clast sample can be attributed to the high strength of the Brazil clasts themselves with

428 low H_2O content. The fact that they survive deformation as more or less rigid particles implies

429 that they have not become sufficiently hydrated. Only limited recrystallization takes place at

430 their margins, where tails of recrystallized quartz grains develop (**Figs. 5-6a,b and 14**). The

431 CPO of their recrystallized grains is oriented synthetically with respect to the imposed shear

432 sense (dextral; **Figure 14**), i.e. similar to that of weaker material of other samples.

433 Applying the empirical quartz flow law by Hirth et al. (2001), and the Paterson & Luan

434 (1990) flow law (for silicic acid), we estimated the differential stress of our quartz matrix for

435 strain rate values of $2*10^{-5}s^{-1}$. Both flow laws predict lower shear stresses ($\Delta\sigma/2$) than our

436 experimental values for pure matrix (111 MPa and 178 MPa versus observed ~200 MPa) but

437 the values are not far off (yellow star and red dot in **Figure 2**).

438 **4.2 Effect of H_2O on deformation**

439 Our samples are deformed by crystal-plastic processes, so that they can be compared with the

440 different deformation regime defined in Hirth and Tullis (1992). Even though Brazil and

441 Hyuga porphyroclasts were deformed at the same P and T, the degree and mechanism of

442 recrystallization was quite different in the two materials.

443 Dry Brazil porphyroclasts show undulatory extinction and abundant deformation lamellae as

444 typical features for dislocation glide with limited recovery or recrystallization in quartz. These

445 features usually occur together with small scale fractures, kinks or short wavelength

446 misorientation bands, and dislocation tangles (Hirth and Tullis, 1992, Trepmann and

447 Stoeckhert, 2013, Stunitz et al., 2017) and can be compared to microstructures observed in the

448 dislocation creep regime 1 of Hirth and Tullis (1992). The presence of small recrystallized

449 grains limited to prophyroclasts rims suggests the onset of subgrain rotation recrystallization.

450 Recrystallized tails at porphyroclasts form a CPO similar to the matrix CPO (**Figure 13**),

451 consistent with activation of slip on the basal <a> system (Schmidt and Casey, 1986; Law,

452 1990).

453 Deformed milky Hyuga quartz shows very different microstructures. The shape of highly

454 elongated Hyuga porphyroclasts can be compared with natural quartz aggregates deformed at

455 mid-greenschist conditions (Law, 1984) or with experimentally deformed Black Hill Quarzite

456 (BHQ) described in regime 2 by Hirth and Tullis (1992) or by Hirth et al., (2001). These

457 elongated grain aggregates are recrystallized to a great extent (**Figs. 6 and 12**). Similar

458 microstructures, and corresponding activated slip systems, are reported also for BHQ

459 (Heilbronner and Tullis, 2006) deformed at higher temperatures and higher strain rates.

460 According to our microstructural observations and CPO, recrystallization took place by

461 subgrain rotation. The development of a common CPO for recrystallized porphyroclasts and

462 matrix indicates that deformation is rather homogenously accommodated within the whole

463 system and dominated by basal <a> slip.

464 The difference between Brazil porphyroclasts, deforming with limited recrystallization, and

465 Hyuga porphyroclasts, pervasively recrystallized by subgrain rotation, can only be explained

466 by their original difference in H_2O content. Our observations further support the effect of H_2O

467 on enhancing microstructural development and recrystallization proposed by Jaoul et al.

468 (1984), Tullis and Yund (1989) and Hirth and Tullis (1992).

469 Most samples converge to a similar strength after a shear strain of ~3 and recrystallization of

470 large volume fractions of the samples (**Figure 2**), even though the initial concentrations of

471 H_2O differed (**Figs. 9 and 11, Table 1**). Some of the main parameters controlling strength are

472 therefore grain size and H_2O distribution, and we can deduce that weakening in experiments

473 with Hyuga porphyroclasts is due to grain size reduction and fluid redistribution as a

474 consequence of dynamic recrystallization.

475 **4.3 Evolution of H_2O with deformation**

476 **4.3.1 H_2O speciation**

477 In addition to the "broad" band of molecular H_2O in the range 2800-3800 cm^{-1}, our samples

478 show a large set of secondary, discrete absorption bands distributed between 3660 and 3300

479 cm^{-1} (**Figs 8-9 and 10 and Table 3**). Most of these bands were not present in the original

480 material and appear after deformation.

481 **4.3.1.1 – Absorption band at 3595 cm^{-1}.**

482   The band 3595 cm^{-1} has been detected in different kinds of natural clear quartz and

483   natural/synthetic amethyst (e.g. (Kats, 1962; Aines and Rossman, 1984; Rovetta, 1989;

484   Kronenberg, 1994), and in natural deformed and then annealed quartzite (Niimi et al., 1999).

485   The common interpretation is that H^{+} charge compensates for Al^{3+} substituting for Si^{4+}.

486   Gleason and DeSisto (2008) described this band in pegmatitic quartz and quartz ribbons,

487   giving the same interpretation.

488   In our experiments, the band at 3595 cm^{-1} is not detected in all samples but it is strictly

489   correlated with attaining P and T and most importantly with deformation. This band is first

490   identified in all matrix analyses (**Figure 8a**), while it is absent in the IR spectra of

491   undeformed Brazil quartz (**Figure 8b**). In Hyuga porphyroclasts, it is not observed at hot-

492   pressed conditions, but it develops after deformation, when porphyroclasts are pervasively

493   recrystallized (**Figure 9**. The band is also observed in Brazil porphyroclasts, but exclusively

494   in their recrystallized tail (**Figure 10b,f**). The 3595 cm^{-1} band is therefore closely associated

495   with recrystallized aggregates of grains, suggesting that the OH species of this band are

496   associated with grain or perhaps subgrain boundaries.

497   Several studies on quartz IR spectra in naturally-deformed rocks further substantiate the

498   connection between a discrete absorption band near 3600 cm^{-1} and recrystallization

499   microstructures. Quartz in mylonites from Sambagawa metamorphic rocks in Japan

500   (Nakashima et al., 1995) and the western Adirondack in the USA (Gleason and DeSisto,

501   2008) show a discrete absorption band around 3600 cm^{-1}. Such a peak is absent in other

502   mylonites, such as granite mylonite in the vicinity of the Median Tectonic Line in Japan

503   (Nakashima et al., 1995; Niimi et al., 1999). However, in these samples it is not clear whether

504   grain boundaries were analyzed by FTIR in addition to grain interiors. The speciation of OH

505   in quartz at subgrain/grain boundaries may be related to silanols at the quartz surface,

506   although the corresponding absorption bands are reported at slightly higher wavenumbers

507   (e.g. 3627 and 3649 cm-1, see the review in (Kronenberg, 1994)) than the ~3595 cm^{-1} peak

508   observed in our study. In summary, a strong connection between increased surface area by

509   recrystallization microstructure and 3595 cm^{-1} absorption band is clear from this study, but

510   the nature of this OH absorption band requires further work.

511   **4.3.1.2 – Absorption band at 3585 cm^{-1}**

512   The absorption band at 3585 cm^{-1} exists in both, Hyuga and Brazil porphyroclasts after

513   deformation (**Figs. 9a,b and 10**). This band has been observed in different materials as

514   amethyst (Kronenberg, 1994, Chakraborty and Lehmann 1976), metamorphic cherts (Ito and

515   Nakashima, 2002), chalcedony (Frondel, 1982; Graetsch, 1985,1987), flint (Graetsch, 1987),

516   agate (Yamagishii et al., 1997) and synthetic quartz (Stalder and Konzett, 2012) Wood, 1960,

517   Kats, 1962; Aines and Rossman, 1984; Cordier and Doukhan, 1989; Chakraborty and

518   Lehmann, 1976; Paterson, 1986; Rovetta, 1989). In experiments of hydrothermal growth of

519   quartz, the intensity of the band increases with pressure and H_2O activity in the surrounding

520   fluid phase (Stalder and Konzett, 2012). A connection of this 3585 cm^{-1} absorption band to

521   deformation was established in deformation experiments (Stünitz et al., 2017), where the

522   development of 3585 cm^{-1} band is confined to deformed parts of single quartz crystals. In

523   addition, a band at 3580 cm^{-1} was observed to develop after annealing of quartz at high

524   temperature (Cordier and Doukhan, 1991; Rovetta et al., 1986). In the latter set of

525   experiments, it was correlated with the formation and healing of cracks during annealing,

526   while no cracks were reported in the former study. Stünitz et al. (2017) suggest that the 3585

527   cm^{-1} band may record OH-defects associated with dislocations. The systematic association

528   between this band and deformation microstructures is also apparent in our samples. This

529   band, absent in "as-is" Hyuga milky quartz samples, appears after both, hot-pressing and

530   deformation (**Figure 10a**), while in Brazil quartz it is observed only in unrecrystallized but

531   deformed (e.g. lamellae) porphyroclasts cores (**Figure 10f**). This close connection to

532   microstructures supports the conclusion by (Stünitz et al., 2017) that the band 3585 cm^{-1} is

533   caused by structurally bond OH at dislocations.

534   **4.3.1.3 – Absorption bands at 3382 cm^{-1} and at 3363 cm^{-1}:**

535   The sharp absorption bands at 3382 cm^{-1} and at 3363 cm^{-1} are specific to the nature of the

536   experimental material, either Hyuga or Brazil quartz.

537   The absorption band at ~3380 cm^{-1} is systematically observed in Hyuga milky quartz before

538   and after deformation. It has been detected in quartz grains of gneiss (Gleason and DeSisto,

539   2008) and in cherts (Ito and Nakashima, 2002) and is attributed by several authors to OH

540   groups bonded with Al^{+3} substituting for Si (Pankrath, 1991; Stalder and Konzett, 2012)

541   Kronenberg, 1994; Suzuki and Nakashima, 1999; Gleason and DeSisto, 2008). This

542   interpretation is supported in our case by the high content of aluminum in Hyuga quartz

543   (Raimbourg et al., 2015).

544   The band at 3363 cm^{-1} is observed only in deformed and recrystallized Brazil quartz, either in

545   the matrix (**Figure 9a**) or at recrystallized tails of porphyroclasts (e.g. **Figure 11**). While it is

546   generally assigned to surface Si-OH groups (Yamagishi et al., 1997), our study does not yield

547   further clues to this attribution.

548   To summarize, we infer that three different species of H_2O are observed after deformation.

549   The first one is molecular H_2O incorporated in porphyroclasts on the form of fluid inclusions,

550   represented by the broad absorption band between 2800 and 3800 cm^{-1}. The second type of

551   H_2O is stored in grain boundaries as a result of recrystallization processes. It is represented by

552   the discrete band at 3595 cm^{-1} corresponding to structurally bond OH-defects. The third type

553   of H_2O is characterized by the discrete band at 3585 cm^{-1} and is probably due to OH-defects

554   on dislocations.

555   **4.3.2 Mechanisms of H_2O incorporation and expulsion**

556   H_2O content in "as-is" Hyuga clasts is estimated at ~22,900 H/10^{6}Si. It decreases first with

557   the application of temperature and pressure to ~12,000 H/10^{6}Si (hot-pressed conditions), and

558   then further decrease to ~2,300 H/10^{6}Si after deformation of γ~4 (**Table 1 and figs. 1b,c,d**

559   **and 10**). The expulsion of H_2O during the application of pressure and temperature does not

560   proceed through recrystallization, as the corresponding new grains were not observed (**Figure**

561   **1c**). In the absence of significant deformation and formation of grain boundaries through

562   recrystallization, the expulsion of H_2O is probably caused by micro-fractures draining fluids

563   from inclusions. One driving force for fracturing during the rise in P and T conditions is the

564   ΔP between the fluid pressure in the inclusions initially present (imposed by the fluid

565   isochoric line) and the confining pressure (experimentally imposed). Decrepitation of fluid

566   inclusions is observed for relatively low ΔP of less than a couple of 100 MPa in experiments

567   (Hall and Sterner, 1993; Vityk and Bodnar, 1995). Furthermore, the initial assembly has a

568   relatively large porosity and heterogeneous grain size distribution (clast + matrix). The

569   application of P and T results in compaction, hence in local stress concentration, which may

570   result in fracturing that may drain fluid inclusions. These fractures are not easily observable

571   because they are systematically healed at high pressure and temperature (Tarantola et al.,

572   2010).

573   During subsequent plastic deformation, dynamic recrystallization (**Figs. 6-7-13**) involving

574   formation and mobility of grain boundaries, provides an efficient process to further decrease

575   the H_2O concentration in the quartz porphyroclasts (**Figure 14a**). Grain boundary mobility

576   has an important effect on modification of volume and distribution of fluid inclusions in

577   experiments (Olgaard et FitzGerald, 1993; Schmatz et Urai, 2010). Observations in natural

578 samples (e.g. Kilian et al., 2016) are consistent with experimental ones. In domains where the

579 Hyuga quartz recrystallized in nature as a result of deformation, the number of fluid

580 inclusions, hence the H_2O content, is strongly decreased (Palazzin et al., 2016). Similarly, Ito

581 and Nakashima (2002) show a strong decrease in the total H_2O content with increasing

582 recrystallization. This implies that extensively recrystallized "dry" porphyroclasts in natural

583 shear zones might have been initially wet.

584 In contrast to Hyuga porphyroclasts, "as-is" Brazil porphyroclasts have a very low initial H_2O

585 content (~260 H/10^6Si). After deformation, both, slightly deformed cores and strongly

586 recrystallized domains, show a significant increase in H_2O: up to 640 and 950-1530 H/10^6Si,

587 respectively (**Table 1**, **Figures 11-14a**). Their final content is similar to the hydrated matrix,

588 which indicates a transfer of H_2O from the matrix to the porphyroclasts during deformation.

589 The process responsible for the increased H_2O content of recrystallized tails of Brazil

590 porphyroclasts is probably identical to that of Hyuga clasts inferred above. The transfer of

591 H_2O to the unrecrystallized cores of Brazil porphyroclasts is probably caused by

592 microcracking as inferred by Kronenberg et al., (1986); Rovetta et al., (1986); Gerretsen et al.,

593 (1989) and Cordier and Doukhan (1989, 1991). The H_2O uptake by non-recrystallized cores

594 of Brazil porphyroclasts, has a limited weakening effect, as attested by the higher strength of

595 samples with a high content of Brazil porphyroclasts (**Figure 2**). Their final H_2O content,

596 ~640H/10^6 Si, is nevertheless higher than the minimum amount of H_2O in wet synthetic

597 quartz (~200 H/10^6 Si) necessary for weakening of these crystals (Kekulawala et al., 1978,

598 1981).

4.3.3 H_2O budget

4.3.3.1 Concentration and distribution of H_2O

601 We measured relatively large and variable (from ~810 to ~3710 H/10^6Si) concentrations of

602 H_2O in the deformed quartz assemblies (**Table 1**). The large variability reflects first the

603 difference in initial H_2O content: in deformation experiments with Hyuga porphyroclasts, the

604 final H_2O content is between ~1470 and 3710 H/10^6Si, while in experiments with Brazil

605 porphyroclasts, or pure matrix, the final H_2O content is between ~640 and 1530 H/10^6Si.

606 Hyuga porphyroclasts, with their stored high H_2O content in fluid inclusions, act as an

607 additional source of H_2O.

608 The experiments were carried out to large shear strain in an attempt to reach some steady-state

609 of the microstructure and H_2O concentration. The flat portions of σ-ε curves do not reach

610 perfect steady-state, but the convergence of strengths of most samples indicates that some

611 final stage of the microstructural development has been reached. In order to find a physical

612 meaning of the H_2O concentration in experiments with Hyuga porphyroclasts, we need to

613 consider where the H_2O is stored, as the IR analysis window size (50x50µm) is larger than the

614 grain size, so that the analyses include grain interiors and grain boundaries.

615 In experiments in quartzite of a large grain size, carried out at the same P-T conditions as

616 ours, a strain rate of $10^{-6}s^{-1}$ and with 0.3 wt% H_2O (Post and Tullis, 1998), the H_2O content in

617 quartz interiors is ~800 $H/10^6Si$, i.e. considerably lower than that in the finely recrystallized

618 Hyuga material, in spite of the very large amount of initially added H_2O (0.3 wt% $H_2O \approx$

619 20,000$H/10^6Si$). In natural mylonite deformed at 800°C and 800MPa, the intracrystalline H_2O

620 content is ~320 $H/10^6Si$ (Gleason and DeSisto, 2008)). A compilation of data of natural

621 quartz deformed in nature and in experiments, shows that intragranular H_2O is significantly

622 lower than bulk measurements, which include the contribution of H_2O at grain boundaries

623 (Kilian et al., 2016). This hypothesis is supported by direct FTIR transects across grains and

624 their boundaries (Post and Tullis, 1998), or by the inverse relationship, in various

625 metamorphic rocks, between the grain size of a rock and the H_2O volume that can be stored in

626 the grain aggregate (Ito and Nakashima, 2002).

627 The concentration of H_2O stored in the grain boundaries of the recrystallized material varies

628 systematically; in experiments with 30% or 70% of Hyuga porphyroclasts, the recrystallized

629 porphyroclasts yield an approximately uniform content of ~2300 $H/10^6Si$. The matrix

630 contains similar amounts of H_2O (~1500 and 2900 $H/10^6Si$). These matrix H_2O contents are

631 systematically larger than in the 100% matrix experiment (~800 $H/10^6Si$), despite the same

632 amount of initially matrix-added water. Thus, H_2O is redistributed from Hyuga porphyroclasts

633 to the matrix producing a uniform range of H_2O contents in Hyuga porphyroclasts and matrix.

634 The H_2O concentration tends to some "equilibrium" concentration, similar to the

635 microstructural evolution which tends to some final "equilibrium" state (**Figure 14a**).

636 **4.3.3.2 Shear bands: evidence for excess H_2O**

637 Shear bands are primarily observed in experiments with Hyuga porphyroclasts and are

638 composed of small faceted quartz grains surrounded by void space (**Figure 7c**). IR

639 measurements show that they contain a significantly larger amount of H_2O than the

640 surrounding matrix (**Table 1**). Their CPO is also different from the surrounding quartz matrix

641 (**Figure 12**). The grain shapes, presence of voids between crystals, and the different crystal

642 orientations from host quartz suggest growth of these quartz grains in a pore space filled with

643   fluid during deformation at high P and T. These shear bands appear to be the locations where

644   excess free fluid phase is stored.

645   **4.3.4 H_2O stored in the grain boundary region**

646   We observed that the deformed quartz aggregates develop towards a common microstructure

647   (**Figs. 11-12 and 13**), strength (**Figure 2**), and H_2O content of the matrix, clasts, and

648   recrystallized material regardless of the initial starting material and relative clast contents

649   (**Figure 14a**). The redistribution of H_2O mainly takes place by recrystallization and formation

650   of new grain boundary area. If it is assumed that the largest part of the H_2O is distributed

651   along the grain boundary regions (the grain interiors cannot store a large amount of H_2O as

652   fluid inclusions because the grain size is below 10 μm), then the volume fraction of H_2O in

653   the quartz aggregate can be plotted against the grain boundary area per analyzed volume

654   (**Figure 14b**). The volume fraction of H_2O is measured by FTIR (**Table 1**), and the grain

655   boundary density (length per surface) is determined by EBSD in the deformed microstructures

656   (**Figs. 11-12 and 13, Table 4**). A similar approach was taken by (Ito and Nakashima, 2002),

657   who used modeled average grain sizes instead of measured boundary fractions. As a result,

658   the pure matrix and the matrix with Brazil clasts have the same nominal grain boundary

659   widths of ~0.7 nm, whereas the matrix with Hyuga clasts has a grain boundary width which is

660   more than twice this width (~1.7 nm; **Figure 14b**). Realistic grain boundary widths have been

661   determined to be ~0.5 nm for feldspar (Hiraga et al., 2004) and ~1nm for pyroxene

662   (Raimbourg et al., 2011), of similar magnitude to those determined here for quartz. The

663   physical state of H_2O stored at grain boundaries is not established, nor the precise nature of

664   the grain boundary itself (Raimbourg et al., 2011). Two types of models are usually proposed

665   for H_2O along the grain boundary: (1) A thin molecular film or (2) A "channel-island"

666   structure, where domains of thin film ("islands") are separated by channels where the

667   thickness of H_2O is larger (e.g. (Den Brok, 1998; Nakashima, 1995)). Our results cannot

668   resolve the details of H_2O distribution along grain boundary, and the method employed here is

669   neither appropriate nor intended for an exact determination of a grain boundary width. The

670   "nominal boundary width" obtained here is merely a measure of the H_2O storage in the grain

671   boundary region under the assumption that the H_2O is evenly distributed along the grain

672   boundaries with a common grain boundary width (**Figure 14a**).

673   The thicker nominal grain boundary width of the sample with Hyuga clasts and higher H_2O

674   content coincides with the occurrence of shear bands (absent in other samples), which are

675   sites of porosity and thus H_2O storage. It is likely that the nominal boundary width of ~1.7 nm

676   corresponds to the H_2O storage capacity of the grain boundary region. If this storage capacity

677   is exceeded, shear bands may develop. This process accounts for the fact that shear bands

678   develop principally in the material with the highest initial H_2O content (i.e. in the samples

679   with Hyuga porphyroclasts). Riedel shear bands, formed during deformation and acting as

680   drains to collect the H_2O from the surrounding matrix, have been similarly described in wet

681   (1.3 wt% H_2O) Dover flint experiments (Schmocker et al., 2003).

682   The shear bands do not have a weakening effect on the bulk sample: The sample with 70%

683   Hyuga clasts and the highest H_2O content is not weaker than others (**Figure 2**). The lack of

684   weakening by shear bands can be explained by a lack of simple connectivity of these bands on

685   the sample scale (Pec et al., 2016; Marti et al., 2017).

686   If H_2O is principally stored at grain boundaries, the storage capacity of the grain aggregate is

687   controlled by the grain size distribution and evolution. The process of redistribution of H_2O

688   takes place by different processes of microcracking (including fluid inclusion decrepitation)

689   and formation of grain boundaries by recrystallization. These processes can be observed in

690   natural samples and the H_2O storage capacity will be an important parameter to be determined

691   for deformation in natural samples, too.

692   **5. Conclusions**

693   In this experimental study the mechanical behavior, microstructural evolution, and H_2O

694   content of different starting materials of "wet" quartz converge at higher shear strain at

695   T=800°C, strain rate=$5*10^{-5}$ s^{-1} and Pc=1.5GPa. From these results we draw several

696   conclusions:

697   • The high crystalline H_2O content, initially present in the form of fluid inclusions in

698   wet quartz, is responsible for enhancing the recrystallization rate, in contrast to

699   initially dry crystals that do not recrystallize extensively.

700   • Sharp absorption bands at 3585 cm^{-1} and 3595 cm^{-1} develop during deformation. The

701   occurrence of the 3585 cm^{-1} band is consistent with dislocation-bound OH, whereas

702   the 3595 cm^{-1} band most likely indicates OH adsorbed at grain boundaries.

703   • Recrystallization results in a clear decrease in H_2O concentration in quartz crystals

704   initially rich in fluid inclusions, whereas H_2O uptake in initially dry crystals takes

705   place by microcracking.

706   • In the deformed and recrystallized assemblies, most H_2O is stored in the grain

707   boundary region. The amount that can be stored in the grain boundary (i.e. the storage

708   capacity) is limited and corresponds to a nominally ☐1.7 nm thick grain boundary

22

709   region. H_2O in excess of this nominal thickness is drained into micro-veins, formed as

710   dilatant synthetic shear bands.

711   • These dilatant shear bands do not control the strength of samples as they are not

712   simply connected.

Aines, R.D., Rossman, G.R. (1984) Water in minerals? A peak in the infrared. J. Geophys. Res. Solid Earth 89, 4059–4071. doi:10.1029/JB089iB06p04059

Bakker, R.J. & Jansen, J.B.H. (1994) Contr. Mineral. and Petrol. 116: 7. doi.org/10.1007/BF00310686.

Blacic, J. D., and J. M. Christie (1984), Plasticity and hydrolytic weakening of quartz single crystals, J. Geophys. Res. Solid Earth, 89(B6), 4223–4239.

Chakraborty, D. & Lehmann, G. (1976). Distribution of OH in synthetic and natural quartz crystals. Journal of Solid State Chemistry 17, 305–311.

Christie, J. M., D. T. Griggs, and N. L. Carter (1964), Experimental evidence of basal slip in quartz, J. Geol., 734–756.

Cordier, P. and Doukhan, J.C. (1989) Water solubility in quartz and its influence on ductility. Eur. J. Mineral. 1, 221-237.

Cordier, P. and Doukhan, J.C. (1991) Water speciation in quartz: a near infrared study. American Mineralogist 76, 361-369.

de Ronde, A.A., Stünitz, H., Tullis, J. and Heilbronner, R. (2005) Reaction-induced weakening of plagioclase–olivine composites. Tectonophysics 409, 85-106.

Den Brok, B. (1998) Effect of microcracking on pressure-solution strain rate: The Gratz grain-boundary model. Geology 26, 915-918.

den Brok, B., J. Meinecke, and K. Roller (1994), Fourier transform IR-determination of intragranular water content in quartzites experimentally deformed with and without added water in the ductile deformation field, J. Geophys. Res., 99, 19,821–19,828.

Doukhan and Trépied, 1985. J.C. Doukhan, L. TrépiedPlastic deformation of quartz single crystals. Bull. Minér., 108 (1985), pp. 97-123.

Fitz Gerald, J.D., Boland, J.N., McLaren, A., Ord, A. and Hobbs, B.E. (1991) Microstructures in water-weakened single crystals of quartz. J. Geophys. Res. 96, 2139-2155.

Frondel, C. (1982), Structural hydroxyl in chalcedony (type B quartz), Am. Mineral., 67, 1248–1257.

Gerretsen, J., Paterson, M.S. and McLaren, A.C. (1989) The uptake and solubility of water in quartz at elevated pressure and temperature. Phys. Chem. Minerals 16, 334-342.

Gleason, G.C. and DeSisto, S. (2008) A natural example of crystal-plastic deformation enhancing the incorporation of water into quartz. Tectonophysics 446, 16-30.

Graetsch, H., Floerke, O.W., and G. Miehe (1985), The nature of water in chalcedony and opal-C from Brazilian agate geodes, Phys. Chem. Miner., 12(5), 300–306.

Graetsch, H., Floerke, O.W., and G. Miehe (1987), Structural defects in microcrystalline silica, Phys. Chem. Miner., 14(3), 249–257.

Griggs, D.T. (1967) Hydrolytic weakening of quartz and other silicates. Geophys. J. Roy. Astron. Soc. 14, 19-31.

Griggs, D.T. (1974) A model of hydrolytic weakening of quartz. J. Geophys. Res. 79, 1653-1661.

Griggs, D.T. and Blacic, J.D. (1965) Quartz: Anomalous weakness of synthetic crystals. Science 147, 292-295.

Hall, D.L. and Sterner, S.M. (1993) Preferential water loss from synthetic fluid inclusions. Contrib. Mineral. Petrol. 114, 489-500.

Hanmer, S. (1984b) The potential use of planar and elliptical structures as indicators of strain regime and kinematics of tectonic flow. Geol Surv Can Pap 84:133–142

Heilbronner, R., Tullis, J. (2006) Evolution of c axis pole figures and grain size during dynamic recrystallization: results from experimentally sheared quartzite. Journal of Geophysical Research-Solid Earth 111 (B10), B10202.

Heilbronner, R., and S. Barrett (2014), Image Analysis in Earth Sciences, pp. 520, Springer, Berlin.

Heilbronner, R. and Kilian, R. (2017) The grain size(s) of Black Hills Quartzite deformed in the dislocation creep regime, Solid Earth, 8, 1071–1093, **https://doi.org/10.5194/se-8-1071-2017**,

Hielscher, R., and H. Schaeben (2008), A novel pole figure inversion method: Specification of the MTEX algorithm, J. Appl. Crystallogr., 41, 1024–1037, doi:10.1107/S0021889808030112. [Available at https://mtex-toolbox.github.io/.]

Hiraga, T., Anderson, I.M. and Kohlstedt, D.L. (2004) Grain boundaries as reservoirs of incompatible elements in the Earth's mantle. Nature 427, 699-703.

Hirth, G. and Tullis, J. (1992) Dislocation creep regimes in quartz aggregates. J. Struct. Geol. 14, 145-159.

Hirth, G., Teyssier, C., Dunlap, J.W., 2001. An evaluation of quartzite flow laws based on comparisons between experimentally and naturally deformed rocks. Int. J. Earth Sci. 90, 77–87. http://dx.doi.org/10.1007/s005310000152.

Ito, Y. and Nakashima, S. (2002) Water distribution in low-grade siliceous metamorphic rocks by micro-FTIR and its relation to grain size: a case from the Kanto Mountain region, Japan. Chem. Geol. 189, 1-18.

Jaoul, O., Tullis, J. and Kronenberg, A.K. (1984) The effect of varying water contents on the creep behavior of Heavitree quartzite. J. Geophys. Res. 89, 4298-4312.Kats, A. (1962). Hydrogen in alpha quartz. Philips Res. Rep. 17, 1–31; 133–195; 201–279.

Kekulawala, K.R.S.S., Paterson, M.S. and Boland, J.N. (1978) Hydrolytic weakening in quartz. Tectonophysics 46, T1--T6.

Kekulawala, K.R.S.S., Paterson, M.S. and Boland, J.N. (1981) An experimental study of the role of water in quartz deformation, in: Carter, N.L., et al. (Eds.), Mechanical behavior of crustal rocks, Geophys. Monogr. Ser., vol. 24. AGU, Washington, D. C., pp. 49-60.

Kidder, S., G. Hirth, J. P. Avouac, and W. Behr (2016), The influence of stress history on the grain size and microstructure of experimentally deformed quartzite, J. Struct. Geol., 83, 194–206.

Kilian, R., Heilbronner, R., Holyoke III, C.W., Kronenberg, A.K. and Stünitz, H. (2016) Dislocation creep of dry quartz. J. Geophys. Res. 121, 3278-3299.

Kilian, R., Heilbronner, R. (2017) Analysis of crystallographic preferred orientations of experimentally deformed Black Hills Quartzite Solid Earth, 8, 1095–1117, 2017.https://doi.org/10.5194/se-8-1095-2017

Kohlstedt, D. L., Evans, B. & Mackwell, S. J. Strength of the lithosphere: Constraints imposed by laboratory experiments. J. Geophys. Res. 100, 17587–17602 (1995).

Kronenberg, A.K. and Tullis, J. (1984) Flow strengths of quartz aggregates: Grain size and pressure effects due to hydrolytic weakening. J. Geophys. Res. 89, 4281-4297.

Kronenberg, A., S. Kirby, R. Aines, and G. Rossman (1986), Solubility and diffusional uptake of hydrogen in quartz at high water pressures: Implications for hydrolytic weakening, J. Geophys. Res., 91(B12), 2723–2744, doi:10.1029/JB091iB12p12723.

Kronenberg, A.K., Segall, P., Wolf, G.H., 1990. Hydrolytic weakening and penetrative deformation within a natural shear zone. Geophys. Monogr. 56, 21–36.

Law, R. D., Knipe, R. J. & Dayan, H. 1984. Strain path partitioning within thrust sheets: Microstructural and petrofabric evidence from the Moine Thrust zone at Loch Eriboll, northwest Scotland. J. Struct. Geol. 6, 477-497.

Law, R.D., 1990. Crystallographic fabrics: a selective review of their applications to research in structural geology. Geol. Soc. Lond. Spec. Publ. 54, 335–352. doi:10.1144/GSL.SP.1990.054.01.30

Lloyd, G.E., Freeman, B., 1994. Dynamic recrystallization of quartz under greenschist conditions. J. Struct. Geol. 16, 867–881. doi:10.1016/0191-8141(94)90151-1

Mainprice, D. and Jaoul, O. (2009) A transmission electron microscopy study of experimentally deformed quartzite with different degrees of doping. Phys. Earth Planet. In. 172, 55-66.

Marti, S., H. Stünitz, R. Heilbronner, O. Plümper, and M. Drury (2017), Experimental investigation of the brittle-viscous transition in mafic rocks - Interplay between fracturing, reaction, and viscous deformation, J Struct Geol 105:62-70, doi.org/10.1016/j.jsg.2017.10.011.

Menegon, L., P. Nasipuri, H. Stünitz, H. Behrens, and E. Ravna (2011), Dry and strong quartz during deformation of the lower crust in thepresence of melt, J. Geophys. Res., 116, B10410, doi:10.1029/2011JB008371.

McLaren, A.C., Cook, R.F., Hyde, S.T. and Tobin, R.C. (1983) The mechanisms of the formation and growth of water bubbles and associated dislocation loops in synthetic quartz. Phys. Chem. Minerals 9, 79-94.

McLaren, A.C., Fitz Gerald, J.D. and Gerretsen, J. (1989) Dislocation nucleation and multiplication in synthetic quartz: relevance to water weakening. Phys. Chem. Minerals 16, 465-482.

Nakashima, S. (1995) Diffusivity of ions in pore water as a quantitative basis for rock deformation rate estimates. Tectonophysics 245, 185-203.

Nakashima, S., Matayoshi, H., Yuko, T., Michibayashi, K., Masuda, T., Kuroki, N., Yamagashi, H., Ito, Y. and Nakamura, A. (1995) Infrared microspectroscopy analysis of water distribution in deformed and metamorphosed rocks. Tectonophysics 245, 263-276.

Niimi, N., Aikawa, A. and Shinoda, K. (1999) The infrared absorption band at 3596 cm-1 of the recrystallized quartz from Mt. Takamiyama, southwest Japan. Mineral. Mag. 63, 693-701.Olgaard, D.L., Fitz Gerald, J.D., 1993. Evolution of pore microstructures during healing of grain boundaries in synthetic calcite rocks. Contributions to Mineralogy and Petrology 115, 138e154.Palazzin, G., Raimbourg, H., Famin, V., Jolivet, L., Kusaba, Y. and Yamaguchi, A. (2016) Deformation processes at the down-dip limit of the seismogenic zone: The example of Shimanto accretionary complex. Tectonophysics 687, 28-43.

Palazzin, G., Raimbourg, H., Famin, V., Jolivet, L., Kusaba, Y. and Yamaguchi, A. (2016) Deformation processes at the down-dip limit of the seismogenic zone: The example of Shimanto accretionary complex. Tectonophysics 687, 28-43.

Pankrath, R. (1991) Polarized IR spectra of synthetic smoky quartz. Phys. Chem. Minerals 17, 681-689.

Passchier CW, Simpson C (1986) Porphyroclast systems as kinematic indicators. J Struct Geol 8:831–844.

Paterson, M. S. (1986), The thermodynamics of water in quartz, Phys. Chem. Miner., 13(4), 245–255.

Paterson, M. S. (1989), The interaction of water with quartz and its influence in dislocation flow: an overview, Rheol. Solids Earth, 107–142.

Paterson, M. S., B. E. Hobbs, and A. C. McLaren (1972), The plasticity of single crystals of synthetic quartz, Transactions of the American Geophysical Union (USA), American Geophysical Union 53rd Annual Meeting, vol. 53, pp. 514–15, AGU, Washington, D. C., 17–21 Apr.

Pec, M., H. Stünitz, R. Heilbronner, and M. Drury (2016), Semi-brittle flow of granitoid fault rocks in experiments at mid-crustal conditions, J. Geophys. Res. Atmos., 121, 1677–1705, doi:10.1002/2015JB012513.

Post, A. and Tullis, J. (1998) The rate of water penetration in experimentally deformed quartzite: implications for hydrolytic weakening. Tectonophysics 295, 117-137.

Prior, D.J. (1999). Problems in determining the misorientation axes, for small angular misorientations, using electron backscatter diffraction in the SEM. J. Microsc.-Oxford 195, 217–225.

Raimbourg, H., Kogure, T. and Toyoshima, T. (2011) Crystal bending, subgrain boundary development, and recrystallization in orthopyroxene during granulite-facies deformation. Contrib. Min. Petr. 162(5), doi:10.1007/s00410-00011-00642-00413.

Raimbourg, H., Famin, V., Palazzin, G., Mayoux, M., Jolivet, L., Ramboz, C. and Yamaguchi, A. (2018) Fluid properties and dynamics along the seismogenic plate interface. Geosphere: Subduction top to bottom 2 14, 1-23.

Raimbourg, H., Vacelet, M., Ramboz, C., Famin, V., Augier, R., Palazzin, G., Yamaguchi, A. and Kimura, G. (2015) Fluid circulation in the depths of accretionary prisms: an example of the Shimanto Belt, Kyushu, Japan. Tectonophysics 655, 161-176.Raimbourg, H., R. Augier, V.

Famin, L. Gadenne, G. Palazzin, A. Yamaguchi, and G. Kimura (2014), Long-term evolution of an accretionary prism: The case study of the Shimanto Belt, Kyushu, Japan, Tectonics, 33, 936–959, doi:10.1002/2013TC003412.

Richter, B., H. Stünitz, and R. Heilbronner (2016), Stresses and pressures at the quartz-to-coesite phase transformation in shear deformation experiments, J. Geophys. Res. Solid Earth, 121, doi:10.1002/2016JB013084.

Rovetta, M.R., Holloway, J.R. and Blacic, J.D. (1986) Solubility of hydroxyl in natural quartz annealed in water at 900°C and 1.5GPa. Geophys. Res. Lett. 13, 145-148.

Rovetta, M.R., 1989. Experimental and spectroscopic constraints on the solubility of hydroxyl in quartz. Phys. Earth Planet. Inter. 55, 326–334. doi:10.1016/0031-9201(89)90080-0

Rutter, E. H. & Brodie, K. H. Experimental grain size-sensitive flow of hot-pressed Brazilian quartz aggregates. Journal of Structural Geology 26, 2011–2023 (2004).

Saffer, D. M. & Tobin, H. J. Hydrogeology and Mechanics of Subduction Zone Forearcs: Fluid Flow and Pore Pressure. *Annual Review of Earth and Planetary Sciences* 39, 157–186 (2011)

Stalder, R. and Konzett, J. (2012) OH defects in quartz in the system quartz–albite–water and granite–water between 5 and 25 kbar. Phys. Chem. Minerals 39, 817-827.

Schmatz, J., Urai, J.L., 2010. The interaction of fluid inclusions and migrating grain boundaries in a rock analogue: deformation and annealing of polycrystalline camphor-ethanol mixtures. J. Metamorph. Geol. 28, 1–18. doi:10.1111/j.1525-1314.2009.00849.x

Schmid, S.M., Casey, M., 1986. Complete fabric analysis of some commonly observed quartz C-axis patterns. In: Hobbs, B.E., Heard, H.C. (Eds.), Mineral and Rock Deformation: Laboratory Studies. American Geophysical Union Monograph, vol. 36, pp. 263–286.

Schmocker, M. *et al.* Granular flow and Riedel band formation in water-rich quartz aggregates experimentally deformed in torsion. *J. Geophys. Res.* 108, 2242 (2003).

Stipp, M. and Tullis, J. (2003) The recrystallized grain size piezometer for quartz. Geophys. Res. Lett. 30, doi:10.1029/2003GL018444.

Stolper, E., 1982. The speciation of water in silicate melts. Geochim. Cosmochim. Acta 46, 2609–2620. doi:10.1016/0016-7037(82)90381-7

Stünitz, H., Thust, A., Heilbronner, R., Behrens, H., Kilian, R., Tarantola, A. and Fitz Gerald, J. (2017) Water redistribution in experimentally deformed natural milky quartz single crystals— Implications for H2O-weakening processes. J. Geophys. Res. 122, 866-894.

Tarantola, A., Diamond, L.W. and Stünitz, H. (2010) Modification of fluid inclusions in quartz by deviatoric stress I: experimentally induced changes in inclusion shapes and microstructures. Contrib. Mineral. Petrol. 160, 825-843.

Tarantola, A., L. W. Diamond, H. Stünitz, A. Thust, and M. Pec (2012), Modification of fluid inclusions in quartz by deviatoric stress. III: influence of principal stresses on inclusion density and orientation, Contrib. to Mineral. Petrol., 164(3), 537–550.

Trepmann, C. A. & Stöckhert, B. Quartz microstructures developed during non-steady state plastic flow at rapidly decaying stress and strain rate. Journal of Structural Geology 25, 2035–2051 (2003).

Tullis, J. and Yund, R.A. (1989) Hydrolytic weakening of quartz aggregates: The effect of water and pressure and recovery. Geoph. Res. Lett. 16, 1343-1346.

Vityk, M.O. and Bodnar, R.J. (1995) Textural evolution of synthetic fluid inclusions in quartz during reequilibration, with applications to tectonic reconstruction. Contrib. Mineral. Petrol. 121, 309-323.

Yamagishi, H., Nakashima, S., Ito, Y., 1997. High temperature infrared spectra of hydrous microcrystalline quartz. Phys. Chem. Miner. 24, 66–74. doi:10.1007/s002690050018.

Wood, D. L. (1960), Infrared absorption of defects in quartz, J. Phys. Chem. Solids, 13(3), 326–336.

Table 1 - Water content

Sample number	Composition of sample	Condition of sample	Measured material	Thickness (cm)	Abs (cm²)	SD	wt. ppm H₂O	SD	wt. ppm H/10⁶ Si	SD	Number of analyses
457GP	100% matrix	deformed	Matrix	0.0120	11.1	2.90	121	28	807	189	31
starting material	Hyuga porphyroclasts	as-is	Porphyroclast	0.0140	383.5	164.4	3446	1234	22973	8224	16
464GP	Hyuga porphyroclasts	attained P-T conditions	Core of porphyroclast	0.0133	191.2	56.2	1809	516	12058	3448	16
464GP	Matrix with Hyuga porphyroclasts	attained P-T conditions	Matrix	0.0127	63.9	34.7	633	344	4219	2296	10
428GP	Hyuga porphyroclasts	deformed	Porphyroclast	0.005	13.6	5.61	342	141	2278	941	8
428GP	Matrix with Hyuga porphyroclasts	deformed	Matrix	0.005	8.76	1.31	220	33	1469	220	9
428GP	Matrix with Hyuga porphyroclasts	deformed	Shear Bands	0.005	22.1	5.66	556	142	3710	949	12
456GP	Hyuga porphyroclasts	deformed	Recrystallized porphyroclast	0.0141	39,6	7.77	353	76	2355	509	15
456GP	Matrix with Hyuga porphyroclasts	deformed	Matrix	0.013	44.8	14.8	430	129	2868	863	9
starting material	Brazil porphyroclasts	as-is	Porphyroclast	0.0136	4.19	0.9	39	10	258	68	7
426GP	Brazil porphyroclasts	deformed	Core of porphyroclast	0.0123	9.36	6.18	96	68	638	455	13
426GP	Brazil porphyroclasts	deformed	Recrystallized porphyroclast	0.0118	21.5	14.9	229	131	1526	873	11
426GP	Matrix in Brazil sample	deformed	Matrix	0.0131	14.8	5.03	142	45	947	299	12
465GP	Brazil porphyroclasts	deformed	Recrystallized porphyroclast	0.0201	21.5	8.35	135	52	898	348	16
465GP	Matrix in Brazil sample	deformed	Matrix	0.0201	31.9	9.39	200	59	1332	391	24

Table 2-Mechanical Data

Sample number	Composition of sample	% water added	$\dot{\gamma}$ [s^{-1}]	Peak τ [MPa]	γ at peak shear stress	τ at $\gamma = 3$ [MPa]	τ at end [MPa]	γ_{final}
457GP	100% matrix	0.15	2.21×10^{-5}	192	0.61	164	201	4.59
462GP	"	"	2.19×10^{-5}	307	0.78	247	256	3.54
426GP	30% Brazil p.	0.10	2.12×10^{-5}	421	0.81	286	271	3.30
428GP	30% Hyuga p.	0.10	2.08×10^{-5}	245	0.80	247	256	3.14
465GP	70% Brazil p.	0.045	2.17×10^{-5}	645	1.55	553	445	4.31
456GP	70% Hyuga p.	0.045	2.07×10^{-5}	398	0.69	277	292	3.87
464GP	30% Hyuga p.	0.10	0.5	-	-		-	-
459GP	100% matrix	0.15	18	-	-		-	-

Table 3 - Absorption bands

Experiment	Material	Conditions	Absorption [cm^{-1}]						
			3363	3385	3430	3485	3585	3595	3625
-	Hyuga porphyroclasts	as-is		x	x	x			x
464GP	Hyuga porphyroclasts	attained P-T cond.		x	x	x	x		x
456GP	Hyuga porphyroclasts	deformed		x			x	x	
-	Brazil porphyroclasts	as-is				x			
426GP	Brazil porphyroclasts	deformed	x				x	x	
464GP	Matrix in Hyuga assembly	attained P-T cond.		x				x	
456GP	Matrix in Hyuga assembly	deformed		x				x	
426GP	Matrix in Brazil assembly	deformed	x					x	

Table 4- Grain boundary density

Experiment	Composition of sample	Grain boundary density (1/m)
457GP	100% matrix	$4.7 \ 10^5$
456GP	70% Hyuga porphyroclasts	$6.7 \ 10^5$
426GP	30% Brazil porphyroclasts	$6.09 \ 10^5$
465GP	70% Brazil porphyroclasts	$7.75 \ 10^5$

Pc = 1.5 GPa / T= 800°C / $\dot{\gamma}$ = 2.1x10^{-5} s^{-1}

70% Brazil Clasts (465GP)

30% Brazil Clasts
(426GP)

70% Hyuga Clasts
(456GP)

100% Matrix (462GP)

30% Hyuga Clasts (428GP)

100% Matrix (457GP)

Shear stress [MPa]

Shear strain [γ]

σ₁ direction

50 µm

(a) 426GP — alumina piston — 18° — 250 µm

(b) 465GP — alumina piston — 18° — 250 µm

(c) fig. 5a-b — 100 µm

(d) 100 µm

30 % BRAZIL porphyroclasts   70 % BRAZIL porphyroclasts

BRAZIL porphyroclast

HYUGA porphyroclast

30 % HYUGA porphyroclasts

70 % HYUGA porphyroclasts

Brazil matrix

3585
3595
3363
3382
464GP (hot pressed conditions)
456GP (deformed)
457GP (100% matrix-deformed)
426GP (deformed)

Brazil porphyroclasts as-is

3485

Wavenumber (cm⁻¹)

(0001) max 14.0
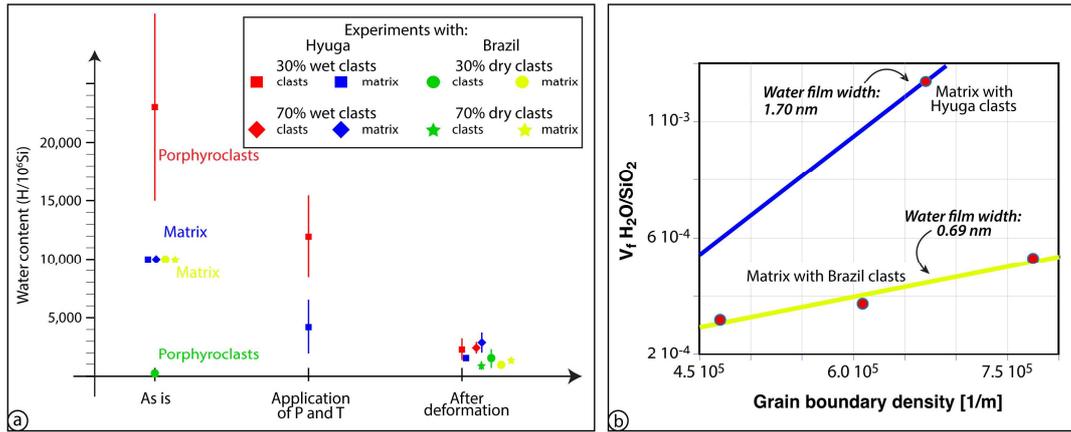
(1120) max 9.7

(1010) max 5.4

- Long-term creep of crustal shear zones is governed by H_2O changes

- H_2O content is not a static value during deformation and metamorphism

- H_2O absorption bands correspond to specific structural positions in quartz